Received 5 December 2003; accepted 9 February 2004; doi:10.1038/nature02411.

1. Greenberg, R. & Nolan, M. C. in *Asteroids II* (eds Binzel, R. P. *et al.*) 778–804 (Arizona Univ. Press, Tucson, 1989).
2. Davis, D. R., Weidenschilling, S. J., Farinella, P., Paolicchi, P. & Binzel, R. P. in *Asteroids II* (eds Binzel, R. P. *et al.*) 805–826 (Arizona Univ. Press, Tucson, 1989).
3. Zappalà, V., Cellino, A., Di Martino, M., Migliorini, F. & Paolicchi, P. Maria's family: physical structure and possible implications for the origin of giant NEAs. *Icarus* **129,** 1–20 (1997).
4. Vokrouhlicky, D. Diurnal Yarkovsky effect as a source of mobility of meter-sized asteroidal fragments. I. Linear theory. *Astron. Astrophys.* **335,** 1093–1100 (1998).
5. Vokrouhlicky, D. A complete linear model for the Yarkovsky thermal force on spherical asteroid fragments. *Astron. Astrophys.* **344,** 362–366 (1999).
6. Vokrouhlicky, D. & Farinella, P. The Yarkovsky seasonal effect on asteroidal fragments: A nonlinearized theory for the plane-parallel case. *Astron. J.* **116,** 2032–2041 (1998).
7. Spitale, J. & Greenberg, R. Numerical evaluation of the general Yarkovsky effect: Effects on semimajor axis. *Icarus* **149,** 222–234 (2001).
8. Bottke, W. F., Jedicke, R., Morbidelli, A., Petit, J. & Gladman, B. Understanding the distribution of near-Earth asteroids. *Science* **288,** 2190–2194 (2000).
9. Bottke, W. F. *et al.* Debiased orbital and absolute magnitude distribution of the near-Earth objects. *Icarus* **156,** 399–433 (2002).
10. Morbidelli, A. & Vokrouhlicky, D. The Yarkovsky-driven origin of near-Earth asteroids. *Icarus* **163,** 120–134 (2003).
11. Pravec, P., Harris, A. W. & Michalowski, T. in *Asteroids III* (eds Bottke, W. F. Jr *et al.*) 113–122 (Arizona Univ. Press, Tucson, 2002).
12. Kryszczyńska, A. *Database of Asteroid Spin Vectors Determinations*. ⟨http://www.astro.amu.edu.pl/Science/Asteroids/⟩ accessed 23 October 2003.
13. Kaasalainen, M. *et al.* Photometry and models of eight near-Earth asteroids. *Icarus* **167,** 178–196 (2004).
14. Magnusson, P. *et al.* in *Asteroids II* (eds Binzel, R. P. *et al.*) 66–97 (Arizona Univ. Press, Tucson, 1989).
15. Rubincam, D. P. Radiative spin-up and spin-down of small asteroids. *Icarus* **148,** 2–11 (2000).
16. Vokrouhlicky, D., Nesvorny, D. & Bottke, W. F. The vector alignments of asteroid spins by thermal torques. *Nature* **425,** 147–151 (2003).
17. Cellino, A., Bus, S. J., Doressoundiram, A. & Lazzaro, D. in *Asteroids III* (eds Bottke, W. F. Jr *et al.*) 633–643 (Arizona Univ. Press, Tucson, 2002).

Acknowledgements This work was supported by MIUR (Italy), KBN (Poland) and the Academy of Sciences (Czech Republic). We thank D. Vokrouhlicky and S. Shore for comments and suggestions.

Competing interests statement The authors declare that they have no competing financial interests.

Correspondence and requests for material should be addressed to P. Paolicchi (paolicchi@df.unipi.it).

Strain-induced metal–insulator phase coexistence in perovskite manganites

K. H. Ahn, T. Lookman & A. R. Bishop

Theoretical Division, Los Alamos National Laboratory, Los Alamos, New Mexico 87545, USA

The coexistence of distinct metallic and insulating electronic phases within the same sample of a perovskite manganite[1–6], such as $La_{1-x-y}Pr_yCa_xMnO_3$, presents researchers with a tool for tuning the electronic properties in materials. In particular, colossal magnetoresistance[7] in these materials—the dramatic reduction of resistivity in a magnetic field—is closely related to the observed texture owing to nanometre- and micrometre-scale inhomogeneities[1–6,8]. Despite accumulated data from various high-resolution probes, a theoretical understanding for the existence of such inhomogeneities has been lacking. Mechanisms invoked so far, usually based on electronic mechanisms and chemical disorder[9–11], have been inadequate to describe the multiscale, multiphase coexistence within a unified picture. Moreover, lattice distortions and long-range strains[12,13] are known to be important in the manganites[14]. Here we show that the texturing can be due to the intrinsic complexity of a system with strong coupling between the electronic and elastic degrees of freedom. This leads to local energetically favourable configurations and provides a natural mechanism for the self-organized inhomogeneities over both nanometre and micrometre scales. The framework provides a physical understanding of various experimental results and a basis for engineering nanoscale patterns of metallic and insulating phases.

Existing theory[9–11] relies predominantly on two very different mechanisms to explain inhomogeneities in manganites: electronic phase separation for nanometre-scale inhomogeneity, and the effects of disorder for micrometre-scale inhomogeneity. Thus two separate mechanisms are invoked to explain two different length scales, in contrast to some experiments[1,2,6,15]. Nanometre-scale inhomogeneities are typically predicted from simulation results of models[9,10] in which the charge density is an order parameter. However, these do not include the long-range Coulomb interaction, and even if it were included, it is not clear whether the inhomogeneity would disappear or whether the system would form polarons or nanometre-scale droplets. Similarly, the random-field Ising models[9,10] proposed for micrometre-scale domains do not capture long-range elastic interactions that are known to be crucial for manganites. Where phenomenological long-range fields are included[11], it is assumed that the metal and insulator states have exactly the same energy in the average random field, even though the two states are not related by symmetry. This leads to a homogeneous phase, contrary to the desired goal of obtaining inhomogeneous states. Although it has been recognized[16–18] that the coupling of spin, charge and lattice distortions together with aspects of nonlinearity are necessary for understanding inhomogeneity in perovskite manganites, few calculations exist that demonstrate how coexistence between metallic and insulating phases arises.

To capture the salient aspects of strong electron–lattice coupling[14] in manganites, we propose a model in which the phase with short- and long-wavelength lattice distortions is insulating, and that without lattice distortion is metallic. Our generic model does not explicitly include other details of perovskite manganites, such as the origin of the short-wavelength lattice distortions (which would be particularly related to oxygen displacements) or magnetic properties[14]. However, we consider that it is the structural aspect that primarily causes the multiphase coexistence, an aspect common to purely strain-based materials such as martensites[19,20] which undergo solid–solid phase transformations. The structural templates then drive novel electronic, magnetic and optical properties in manganites. The explicit inclusion of lattice degrees of freedom, together with the effects of electron–lattice coupling and the use of a single mechanism to obtain both nanometre- and micrometre-scale inhomogeneities, distinguishes our model from other existing models[9–11]. The multiphase coexistence originates from lattice degrees of freedom rather than charge density, so including the Coulomb interaction would not change the qualitative features of our results, particularly if the charge fluctuations on Mn sites are small or screened, as suggested recently[21]. Thus our microscopic model describes submicrometre texture that does not necessarily rely on substantial fluctuations in charge density even at the atomic scale. Separation of lattice distortions into short (s_x and s_y in Fig. 1a) and long (e_1, e_2 and e_3 in Fig. 1a) wavelength modes and constraints amongst them, which mediate long-range anisotropic elastic interactions, have been developed and tested on simple examples[12,13], and are used as a technical tool in our current model for manganites. Our model also provides a basis for understanding other features observed in manganites, such as precursor short-range ordering[8] and quasi-elastic scattering[22,23] near the phase-transition temperature, hysteretic and glassy dynamics[22,24], metastability[25] and a photo-induced insulator–metal transition[26,27].

The lattice distortions in manganites closely follow the state of the outermost shell (e_g) electrons on Mn ions through a Jahn–Teller coupling[14]. If an e_g electron is localized at a Mn site in the insulating phase, the symmetry of the surrounding oxygen octahedron is

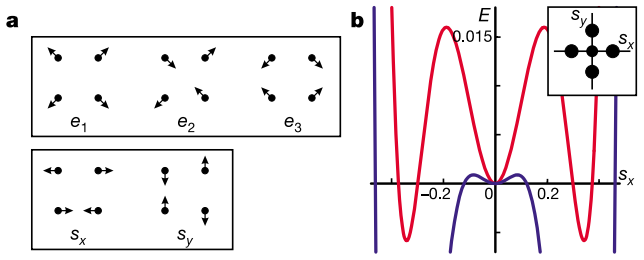

Figure 1 Modes and energy landscape. **a**, Atomic-scale lattice distortion modes (positive) for a monatomic square lattice in two-dimensional (2D) space[12]. **b**, Energy landscape along $s_y = 0$ in $s_x - s_y$ plane for two different positive values of the harmonic modulus for short-wavelength distortion, B, in the energy expression below. The global minimum of the blue curve is at $E = -0.11$. The solid circles in the inset schematically represent the locations of local minima in the $s_x - s_y$ plane. We consider the situation in which the undistorted state itself is a local energy minimum and the distorted state is the global energy minimum. For $B < 0$, the resultant double-well energy potential, for which the undistorted phase is unstable, would merely yield as inhomogeneity a line (a plane in three dimensions, 3D) of atoms instead of submicrometre-sized domains observed by electron microscopy[2]. The energy expression for our 2D model for a square lattice is $E = E_{\text{long}} + E_{\text{short}} + E_{\text{coupling}}$, where $E_{\text{long}} = \Sigma_{\text{sites}}\ A_1 e_1^2/2 + A_2 e_2^2/2 + A_3 e_3^2/2$, and $E_{\text{short}} = \Sigma_{\text{sites}}\ B(s_x^2 + s_y^2)/2 + G_1(s_x^4 + s_y^4)/4 + G_2 s_x^2 s_y^2/2 + H_1(s_x^6 + s_y^6)/6 + H_2 s_x^2 s_y^2(s_x^2 + s_y^2)/6$, and $E_{\text{coupling}} = \Sigma_{\text{sites}}\ C_3(s_x^2 - s_y^2)e_3$. E_{long} contains the harmonic energy for dilatation (e_1), shear (e_2) and deviatoric (e_3) long-wavelength modes, which lead to an anisotropic long-range interaction[29]. The symmetry-allowed energy terms for short-wavelength modes (s_x, s_y) are considered up to sixth order to include features associated with first-order phase transitions. E_{coupling} represents the coupling between short- and long-wavelength modes, where the positive C_3 is the strength of this coupling. In the homogeneous phase, all modes are independent and E can be minimized separately for each mode[12]. Such separate minimization gives $e_1 = e_2 = 0$ and $e_3 = -C_3(s_x^2 - s_y^2)/A_3$, which renormalize the fourth-order coefficients and provide the condition to have both distorted and undistorted phases as local minimum states in the $s_x - s_y$ plane. Our model can be extended to study the effects of other perturbations, such as the size distribution of Re/Ak ions[15,30], substrate-induced strains in thin films, external stress or grain boundaries in polycrystals[1,16,19].

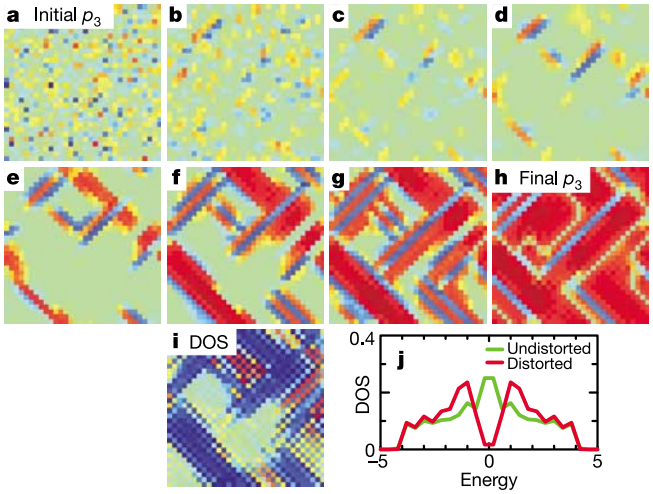

Figure 2 Results of simulations for the shallow local minimum case (blue curve in Fig. 1b) on a 32 × 32 lattice with periodic boundary conditions. **a**, The $p_3 = s_x^2 - s_y^2$ field initial configuration. **b**–**g**, Time-sequence of p_3 during energy relaxation. **h**, Final stable stage. (Dark red and dark blue represent $\pm\ s_0^2$, except in **a** where they correspond to $\pm\ (2.6 s_0)^2$. s_0 is the value of s_x or s_y at the global minimum distorted state.) **i**, Local electronic DOS at $\epsilon_F = 0$ for the distorted pattern in **f** (dark blue and dark red correspond to 0 and 0.5). **j**, Typical local electronic DOS versus electronic energy within the distorted and undistorted regions. The small finite DOS within the gap is due to the exponentially decaying leakage of electronic state from the metallic region: a 'pseudogap'. The distorted lattice with s_x and negative e_3, or equivalently that with s_y and positive e_3 (see Fig. 1a), leads to a gap in the electronic DOS near electronic energy $\epsilon = 0$. Thus, if ϵ_F lies in the gap, the distorted lattice behaves as an insulator. In the structure without distortions, the DOS has no gap, and the electrons are in a metallic state. Crucially, the study of the inhomogeneous phase shown here in **a**–**h** requires that constraints between the distortion variables be satisfied, allowing bonds between atoms to bend but not break[12,13,29]. Elimination of e_1, e_2 and e_3 subject to these constraint equations leads to an energy expression in terms of s_x and s_y, which we numerically minimize using various initial configurations. The electronic properties in **i** and **j** are obtained by numerically solving the SSH hamiltonian on the elastic templates.

lowered from cubic to tetragonal. At low temperatures, the distorted octahedra stack in particular patterns, often referred to as charge and orbital ordering[1]. For example, in $La_{0.5}Ca_{0.5}MnO_3$, the long Mn–O bonds of the elongated octahedra form a zigzag pattern in the x–y plane[28], giving rise to short-wavelength lattice distortions. The stacking of the short Mn–O bonds along the z-direction is responsible for the uniform (or long-wavelength) tetragonal (more accurately orthorhombic) distortion. Such lattice distortions are absent in the metallic phase because the e_g electrons are delocalized.

The coupled short- and long-wavelength modes in the cubic anharmonic elastic energy give rise naturally to an energy 'landscape' with multiple energy minima. A number of experimental results support the presence of metastable states in manganites. For example, magnetic fields[25] or X-rays[26] have been used to convert insulating regions into ferromagnetic metallic ones, which are stable even when the magnetic fields or X-rays are removed. For illustration, we consider here two cases with different harmonic moduli for short-wavelength lattice distortions as shown in Fig. 1b, one giving a shallow (blue curve, a small modulus) and the other a deep (red curve, a large modulus) local minimum for the undistorted phase. Solid circles in the inset represent locations of energy minima for our model in the $s_x - s_y$ space. The modulus can be changed, for example, by varying the average size of the rare-earth (Re) and alkali-metal (Ak) ions, which sensitively alters manganite properties[15].

Figure 2a–h shows the sequential relaxations for the shallow local minimum case starting from random initial s_x and s_y values, corresponding to a rapid cooling of the system from high temperature. The results are represented in terms of $p_3 = s_x^2 - s_y^2$, which serves as an order parameter. Positive (red) and negative (blue) values of p_3 correspond to different orientations of short- or long-wavelength lattice distortions (s_x with negative e_3 and s_y with positive e_3). The short- and long-wavelength mode distortions are simultaneously generated through the minimal symmetry-allowed coupling between e_3 and $s_x^2 - s_y^2$ at each site. The green regions with zero p_3 have no distortions. Most of the region initially relaxes to the undistorted local minimum state, as shown in Fig. 2c and d, because the rapidly fluctuating initial field contains few components of the long-wavelength strain modes, which makes it difficult for the system to reach the global minimum state. However, even in the presence of the random field, there are regions with some correlation, which eventually lead to nanometre-scale nucleating droplets. Comparison of Fig. 2b–d shows that there is a critical strength and size of these droplets, a common feature of first-order phase transitions. However, the long-range nature and anisotropy of the interaction between strain fields[12,13,29] define the nucleation process uniquely. First, the morphology of the nucleated droplets often consists of a pair of strain fields with different orientations (see Fig. 2d) to minimize the energy cost at the boundary between the distorted and undistorted phases. Second, extended long-range correlations along the favoured direction can allow for easy growth of distorted regions (the broad 135-degree $p_3 > 0$ regions in Fig. 2d and e). Third, the nucleated droplets are highly anisotropic, unlike usual first-order phase transitions. These distinct characteristics of elastic nucleation are the probable source of the nanometre-scale

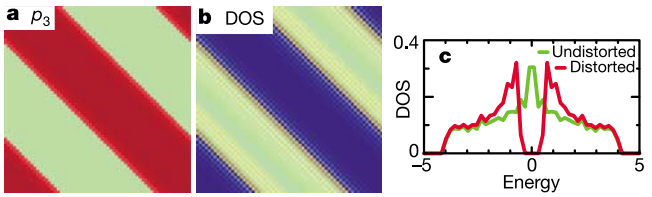

Figure 3 Results of simulations for the deep local minimum case (red curve in Fig. 1b) on a 64 × 64 lattice. **a**, p_3 field for the stable elastic texture (same colour scheme as Fig. 2). **b**, Local DOS configuration at $\epsilon_F = 0$. Blue and green regions are distorted insulator and undistorted metal, respectively. **c**, Typical local DOS versus energy within distorted and undistorted regions. As seen by comparing Figs 2 and 3, the depth of the local energy minimum changes the nature of the inhomogeneity, from nanometre-scale fluctuations to micrometre-scale stable domains. In manganites, the harmonic modulus for the short-wavelength distortions, which changes the depth of the local energy minimum in Fig. 1b, may be varied by changing the size of Re/Ak ions (often parameterized as a 'tolerance factor'[15]). More specifically, the effect of the size of Re/Ak ions[30] on the modulus may be represented through an additional symmetry-allowed coupling $C_1 e_1(s_x^2 + s_y^2)$ in our model. The small-size Re/Ak site ions create an isotropic strain (that is, e_1), which renormalizes the harmonic modulus for the short-wavelength distortion modes through this cubic anharmonic term. Other physics, such as magnetism and kinetic energy of electrons, particularly coupled with the buckling of oxygen octahedra, can also change the effective modulus and the energy landscape.

inhomogeneity seen in manganites, for example, the anisotropic short-range precursor correlations at high temperatures[8] and the quasielastic central peak in neutron scattering near the metal–insulator phase-transition temperatures[22] (analogues of the central peaks in ferroelectrics). Such behaviour is very reminiscent of the precursor embryonic fluctuations observed in martensitic transformations[20].

Figure 2i and j shows the tight-binding electronic structure supported by the lattice distortion template in Fig. 2f. For illustration, we have used a Su–Shrieffer–Heeger (SSH) electron–lattice coupling model[13] (with one electron per site) that linearly incorporates the variation of the electron transfer probability between neighbouring sites due to the changes in interatomic distances. This SSH model, together with the specific coupling between short- and long-wavelength modes mentioned earlier, gives rise to the desired electronic phases for undistorted and distorted structures. The typical local electronic density of states (DOS) versus electronic energy shown in Fig. 2j indeed indicates a metallic local DOS in the undistorted region and a gapped (insulating) local DOS within the distorted region. For the Fermi energy $\epsilon_F = 0$, the local DOS configuration in direct space is shown in Fig. 2i. This illustrates the coexistence of metal (green) and insulator (blue) associated with the elastic texture template, similar to that observed in manganites[2–4].

For the deeper local-minimum case, the simulation of the rapid cooling process from random initial configurations shows characteristic features of metastability or a supercooled state, such as a low probability of creating nucleation droplets. Such slow relaxation dynamics requires extensive computational resources, so we choose instead predesigned initial conditions, such as a sinusoidal spatial variation of s_x or s_y along a 45-degree direction. A typical result in the final p_3 field is shown in Fig. 3a. The regions with large (or small) initial $|s_x|$ or $|s_y|$ transform to a distorted global (or undistorted local) minimum state upon energy minimization. The energy landscape near the undistorted state is deep enough that the coexisting phase of metal and insulator is stable, unlike the shallow local-minimum case above. Such stable coexistence of metallic and insulating domains, which can be as large as several micrometres when simulated on a larger lattice, is similar to the submicrometre size multiphase coexistence observed in $La_{1-x-y}Pr_yCa_xMnO_3$ (ref. 2). Thermal fluctuations at finite temperatures can grow the distorted region slowly—such slow, history-dependent dynamics with time-scales that range from 10–20 min to 2–3 h has been also observed in various manganites[22,24]. Figure 3b and c shows the corresponding electronic inhomogeneities within the SSH model. The local DOS for the sites deep within the domain shows a clear gap near electronic energy $\epsilon = 0$. Thus, for $\epsilon_F = 0$, the metallic and insulating phases coexist with relatively sharp boundaries, as observed in STM images of $Bi_{0.24}Ca_{0.76}MnO_3$ (ref. 4).

A magnetic field is expected to modify the energy landscape in favour of the undistorted ferromagnetic metallic state, which would increase the volume fraction of metallic regions in both the phase with metal–insulator domains (Fig. 3) and the phase with precursor embryonic fluctuations (Fig. 2). In particular, the reduction of the quasi-elastic scattering spectral weight by applied magnetic fields[23] provides evidence for the latter case, and hence percolating conducting paths created by these fields can lead to the observed colossal magnetoresistance. The mechanisms we have proposed here can be applied to describe inhomogeneities in other materials with strong bonding constraints, such as relaxor ferroelectrics and possibly high-transition-temperature (high-T_c) superconducting oxides, where we believe the functionalities are also mediated through self-organized lattice distortions.

The above results show that the micrometre-scale multiphase coexistence is self-organized and is caused by the presence of an intrinsic elastic energy landscape, whereas existing theory[9–11] suggests that the micrometre-scale inhomogeneity originates from the random distribution of Re/Ak ions. The two models make different predictions on engineering patterns of metal and insulator domains. The existing theory requires redistribution of Re/Ak ions to change patterns of multiphase domains. In our model, because the domain formation is self-sustained, external stimuli such as optical lasers, X-rays, or ultrasonic standing waves, can be used to sensitively manipulate patterns of metallic and insulating regions, thus making the control of nano-engineered functional domains in manganites feasible. □

Received 4 November 2003; accepted 23 January 2004; doi:10.1038/nature02364.

1. Salamon, M. B. & Jaime, M. The physics of manganites: structure and transport. *Rev. Mod. Phys.* **73,** 583–628 (2001).
2. Uehara, M., Mori, S., Chen, C. H. & Cheong, S.-W. Percolative phase separation underlies colossal magnetoresistance in mixed-valent manganites. *Nature* **399,** 560–563 (1999).
3. Fäth, M. *et al.* Spatially inhomogeneous metal-insulator transition in doped manganites. *Science* **285,** 1540–1542 (1999).
4. Renner, Ch., Aeppli, G., Kim, B.-G., Soh, Y.-A. & Cheong, S.-W. Atomic-scale images of charge ordering in a mixed-valence manganite. *Nature* **416,** 518–521 (2002).
5. Zhang, L., Israel, C., Biswas, A., Greene, R. L. & de Lozanne, A. Direct observation of percolation in a manganite thin film. *Science* **298,** 805–807 (2002).
6. Mathur, N. & Littlewood, P. Mesoscopic texture in manganites. *Phys. Today* **56,** 25–30 (2003).
7. Jin, S. *et al.* Thousandfold change in resistivity in magnetoresistive La-Ca-Mn-O films. *Science* **264,** 413–415 (1994).
8. Kim, K. H., Uehara, M. & Cheong, S.-W. High-temperature charge-ordering fluctuation in manganites. *Phys. Rev. B* **62,** R11945–R11948 (2000).
9. Moreo, A., Yunoki, S. & Dagotto, E. Phase separation scenario for manganese oxides and related materials. *Science* **283,** 2034–2039 (1999).
10. Dagotto, E., Hotta, T. & Moreo, A. Colossal magnetoresistant materials: The key role of phase separation. *Phys. Rep.* **344,** 1–153 (2001).
11. Burgy, J., Moreo, A. & Dagotto, E. Relevance of cooperative lattice effects and correlated disorder in phase-separation theories for CMR manganites. *Phys. Rev. Lett.* (submitted); preprint at ⟨http://www.arXiv.org/cond-mat/0308456⟩ (2003).
12. Ahn, K. H., Lookman, T., Saxena, A. & Bishop, A. R. Atomic scale lattice distortions and domain wall profiles. *Phys. Rev. B* **68,** 092101 (2003).
13. Ahn, K. H., Lookman, T., Saxena, A. & Bishop, A. R. Microstructural evolution and electronic properties of antiphase boundaries in elastic materials. *Phys. Rev. B* (submitted); preprint at ⟨http://www.arXiv.org/cond-mat/0309328⟩ (2003).
14. Millis, A. J. Lattice effects in magnetoresistive manganese perovskites. *Nature* **392,** 147–150 (1998).
15. Hwang, H. Y., Cheong, S.-W., Radaelli, P. G., Marezio, M. & Batlogg, B. Lattice effects on the magnetoresistance in doped $LaMnO_3$. *Phys. Rev. Lett.* **75,** 914–917 (1995).
16. Mathur, N. D. & Littlewood, P. B. The self-organised phases of manganites. *Solid State Commun.* **119,** 271–280 (2001).
17. Millis, A. J. Towards a classification of the effects of disorder on materials properties. *Solid State Commun.* **126,** 3–8 (2003).
18. Bishop, A. R., Lookman, T., Saxena, A. & Shenoy, S. R. Elasticity-driven nanoscale texturing in complex electronic materials. *Europhys. Lett.* **63,** 289–295 (2003).
19. Podzorov, V., Kim, B. G., Kiryukhin, V., Gershenson, M. E. & Cheong, S.-W. Martensitic accommodation strain and the metal-insulator transition in manganites. *Phys. Rev. B* **64,** 140406 (2001).

20. Seto, H., Noda, Y. & Yamada, Y. Precursor phenomena at martensitic phase transition in Fe-Pd alloy. II. Diffuse scattering and embryonic fluctuations. *J. Phys. Soc. Jpn* **59,** 978–986 (1990).
21. Ferrari, V., Towler, M. & Littlewood, P. B. Oxygen stripes in $La_{0.5}Ca_{0.5}MnO_3$ from ab initio calculations. *Phys. Rev. Lett.* **91,** 227202 (2003).
22. Lynn, J. W. *et al.* Unconventional ferromagnetic transition in $La_{1-x}Ca_xMnO_3$. *Phys. Rev. Lett.* **76,** 4046–4049 (1996).
23. Lynn, J. W. *et al.* Magnetic, structural, and spin dynamical properties of $La_{1-x}Ca_xMnO_3$. *J. Appl. Phys.* **81,** 5488–5490 (1997).
24. Levy, P., Parisi, F., Granja, L., Indelicato, E. & Polla, G. Novel dynamical effects and persistent memory in phase separated manganites. *Phys. Rev. Lett.* **89,** 137001 (2002).
25. Tokura, Y., Kuwahara, H., Moritomo, Y., Tomioka, Y. & Asamitsu, A. Competing instabilities and metastable states in $(Nd,Sm)_{1/2}Sr_{1/2}MnO_3$. *Phys. Rev. Lett.* **76,** 3184–3187 (1996).
26. Kiryukhin, V. *et al.* An X-ray induced insulator metal transition in a magnetoresistive manganite. *Nature* **386,** 813–815 (1997).
27. Fiebig, M., Miyano, K., Tomioka, Y. & Tokura, Y. Visualization of the local insulator-metal transition in $Pr_{0.7}Ca_{0.3}MnO_3$. *Science* **280,** 1925–1928 (1998).
28. Chen, C. H. & Cheong, S.-W. Commensurate to incommensurate charge ordering and its real-space images in $La_{0.5}Ca_{0.5}MnO_3$. *Phys. Rev. Lett.* **76,** 4042–4045 (1996).
29. Lookman, T., Shenoy, S. R., Rasmussen, K. Ø., Saxena, A. & Bishop, A. R. Ferroelastic dynamics and strain compatibility. *Phys. Rev. B* **67,** 024114 (2003).
30. Rodriguez-Martinez, L. M. & Attfield, J. P. Cation disorder and size effects in magnetoresistive manganese oxide perovskites. *Phys. Rev. B* **54,** R15622–R15625 (1996).

Acknowledgements We thank A. Saxena for discussions. The work was supported by the US DOE.

Competing interests statement The authors declare that they have no competing financial interests.

Correspondence and requests for materials should be addressed to K.H.A. (ahn@lanl.gov).

Onset of heterogeneous crystal nucleation in colloidal suspensions

A. Cacciuto, S. Auer* & D. Frenkel

FOM Institute for Atomic and Molecular Physics, Kruislaan 407, 1098 SJ Amsterdam, The Netherlands

* Present address: Department of Chemistry, Cambridge University, Lensfield Road, Cambridge, CB2 1EW, UK

The addition of small 'seed' particles to a supersaturated solution can greatly increase the rate at which crystals nucleate. This process is understood, at least qualitatively, when the seed has the same structure as the crystal that it spawns[1,2]. However, the microscopic mechanism of seeding by a 'foreign' substance is not well understood. Here we report numerical simulations of colloidal crystallization seeded by foreign objects. We perform Monte Carlo simulations to study how smooth spherical seeds of various sizes affect crystallization in a suspension of hard colloidal particles. We compute the free-energy barrier associated with crystal nucleation[3,4]. A low barrier implies that nucleation is easy. We find that to be effective crystallization promoters, the seed particles need to exceed a well-defined minimum size. Just above this size, seed particles act as crystallization 'catalysts' as newly formed crystallites detach from the seed. In contrast, larger seed particles remain covered by the crystallites that they spawn. This phenomenon should be experimentally observable and can have important consequences for the control of the resulting crystal size distribution.

Ostwald's 1897 paper on crystal nucleation[1] contains an interesting remark in the introduction. After explaining that supercooled liquids can be made to crystallize by the introduction of a small seed crystal, Ostwald writes: "I am not aware of any experiments to determine the smallest amount of solid that is needed to make this procedure [that is, the crystallization] succeed".

More than a century has passed since then, and much has been learned about the process of crystal nucleation. But part of the question that Ostwald posed remains unanswered. The classical theory of nucleation provides a natural explanation of why a seed crystal facilitates crystal nucleation[2]: in order to grow, crystallites of the stable phase need to exceed a critical size. Crystallites that are smaller than this 'critical nucleus' dissolve again, crystallites that are larger can grow to a macroscopic size. In the absence of a seed, a rare, spontaneous fluctuation is needed to form a crystal nucleus that exceeds the critical size. However, crystallization can proceed spontaneously if we add a seed crystal that is larger than the critical nucleus to the metastable liquid phase.

But crystallization can also be induced by introducing foreign substances. And for that case, the answer to Ostwald's question is not known. Here we use computer simulations to study how very small foreign objects ('nano-dirt') influence the rate of crystal nucleation. In particular, we consider the effect of spherical seed particles on the crystallization of uncharged, spherical colloids.

First, we consider the effect of a flat wall on crystal nucleation. On an atomic scale, no wall is perfectly flat. But it is relatively straightforward to study colloidal crystallization on surfaces that are flat on the scale of a colloidal particle (50 nm, or more). Experiments[5–7] and simulations[8] show that such a flat wall speeds up colloidal crystallization by many orders of magnitude. Next, consider a smooth, spherical object of finite size. Clearly, if the object is very large, its effect should be similar to that of a hard wall. At the other limit, where the object has the same size as the colloids in the system, the object should have no effect on the nucleation rate.

One might expect that nucleation speeds up monotonically with the size of the spherical seed, but this is not true. Because crystals cannot grow on spheres without generating topological defects[9,10], nucleation of spherical particles on, or near, a sphere with a different size is inhibited. This shows up dramatically in the increase of the crystal nucleation barrier in a system of polydisperse hard spheres[11]. Yet, if we introduce only a single, mismatched sphere in the liquid, then the effect on nucleation is minimal: true, nucleation does not take place very close to this sphere, but the homogeneous nucleation in the rest of the volume is unaffected. To discover the minimum size of a spherical seed that can affect the rate of crystal nucleation,

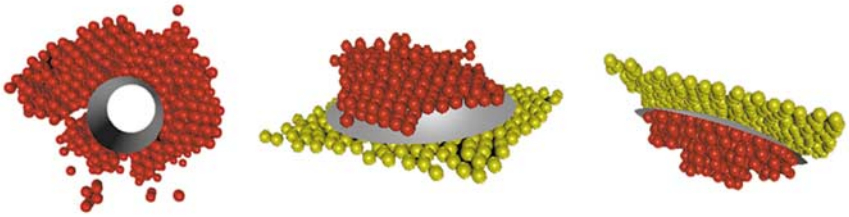

Figure 1 The spontaneous crystallizations of hard-sphere colloids on seed particles. The seed particles are a cylinder ($R_s = 3\sigma$, at $\phi = 0.523$) and a spherical cap ($R_s = 60\sigma$, at $\phi = 0.513$). The middle and right images show nucleation on the convex and on the concave sides of a spherical seed, respectively. To distinguish between the two cases, we cover the bottom (for $\kappa > 0$) or top (for $\kappa < 0$) of the spherical caps with a disordered template to prevent crystallization on that side of the seed.